

## REPORT DOCUMENTATION PAGE

The public reporting burden for this collection of information is estimated to average 1 hour per response, including the time for reviewing instructions, searching existing data sources, gathering and maintaining the data needed, and completing and reviewing the collection of information. Send comments regarding this burden estimate or any other aspect of this collection of information, including suggestions for reducing the burden, to the Department of Defense, Executive Service Directorate (0704-0188). Respondents should be aware that notwithstanding any other provision of law, no person shall be subject to any penalty for failing to comply with a collection of information if it does not display a currently valid OMB control number.

**PLEASE DO NOT RETURN YOUR FORM TO THE ABOVE ORGANIZATION.**

1. REPORT DATE (DD-MM-YYYY)	2. REPORT TYPE	3. DATES COVERED (From - To)		
07-01-2009	Final	September 2005 -September 2008		
4. TITLE AND SUBTITLE Integrated Computational/Experimental Study of Turbulence Modification and Mixing Enhancement in Swirling Jets		5a. CONTRACT NUMBER		
		5b. GRANT NUMBER FA9550-05-1-0485		
		5c. PROGRAM ELEMENT NUMBER		
6. AUTHOR(S) J. Naughton, D. Stanescu, S. Heinz, R. Semaan, M. Stoellinger, and C. Zemtsop		5d. PROJECT NUMBER		
		5e. TASK NUMBER		
		5f. WORK UNIT NUMBER		
7. PERFORMING ORGANIZATION NAME(S) AND ADDRESS(ES) University of Wyoming Department 3295, Mechanical Engineering 1000 E. University Ave., Laramie, WY 82070		8. PERFORMING ORGANIZATION REPORT NUMBER UWAA-2009-01		
		10. SPONSOR/MONITOR'S ACRONYM(S)		
9. SPONSORING/MONITORING AGENCY NAME(S) AND ADDRESS(ES) Air Force Office of Scientific Research John D. Schmisseur, Ph.D. 875 North Randolph Street, Suite 325, Room 3112 Arlington, VA 22203		11. SPONSOR/MONITOR'S REPORT NUMBER(S)		
		12. DISTRIBUTION/AVAILABILITY STATEMENT Approval for public release; distribution is unlimited.		
13. SUPPLEMENTARY NOTES The views and conclusions contained herein are those of the authors and should not be interpreted as necessarily representing the official policies or endorsements, either expressed or implied, of the Air Force Office of Scientific Research or the U.S. Govt.				
14. ABSTRACT Swirling jet flows have been studied experimentally and computationally and the results have been compared with theory. Three-component Laser Doppler Anemometry (LDA) measurements have been carried out for swirling jets of various strengths and swirl distributions. Radial profiles of velocity have been obtained from the jet exit to 50 diameters downstream. The experimental results are consistent with previous results and with similarity theory for weakly swirling turbulent jets. However, the parametric range and spatial domain of the current data set makes it suitable for validation. Computational simulations have also been performed using a combination of Reynolds Averaged Navier-Stokes (RANS) and Large Eddy Simulation (LES) approaches. The results have been validated with experimental data and used to explore the mechanisms behind the increased mixing enhancement observed. The combined experimental/computational effort is still ongoing, but the experiences to date have demonstrated the effectiveness of such an approach.				
15. SUBJECT TERMS Jet Flows, Swirling Jets, Turbulent Jets, Laser Doppler Anemometry, Similarity, Large Eddy Simulation				
16. SECURITY CLASSIFICATION OF: a. REPORT    b. ABSTRACT    c. THIS PAGE		17. LIMITATION OF ABSTRACT	18. NUMBER OF PAGES	19a. NAME OF RESPONSIBLE PERSON Jonathan W. Naughton
U	U	U	UU	19b. TELEPHONE NUMBER (Include area code) (307)766-6284

Integrated Computational/Experimental Study of  
Turbulence Modification and Mixing Enhancement  
in Swirling Jets

J. Naughton, D. Stanescu, S. Heinz,  
R. Semaan, M. Stöellinger, and C. Zemtsop

Report UWAA-2009-01

*Wyoming Active Aero  
University of Wyoming, Laramie, WY 82071*

Final Report for AFOSR Award FA9550-05-1-0485  
For the period August 15, 2005 - August 14, 2008

January 7, 2009

**20090319195**

# 1 Introduction

Swirling jets are important in many applications relevant to the Air Force. For example, swirling flows are often used in combustors to enhance fuel/air mixing. In addition, swirling flows are present in turbomachinery. Swirling jets exhibit more rapid growth rates and higher absolute turbulence in the near field that may be useful for many applications. However, these characteristics also make this flow interesting to study from a fundamental turbulence viewpoint, since these swirling jets exhibit substantial differences from their non-swirling counterparts.

As a result of their unique characteristics, swirling jets have been studied extensively using theoretical, experimental, and numerical approaches. Nonetheless, a complete understanding of their behavior is missing. A comprehensive experimental data set that captures the effects of different swirl profiles and strengths in both the near and far field is needed. In addition, most existing measurement efforts have used hot-wire anemometry rather than LDA. Since LDA is the most appropriate technique for single-point measurements in high turbulence intensity flows, it is used in the present study. Since such data sets are missing, fully validated computations that can assist in understanding the important mechanisms present in the flow are also missing. The combination of such experimental and computational data sets would provide the much needed information to better understand these flows.

Due to the perceived need and our history of working with swirling flows, a combined computational/experimental investigation was undertaken. For the numerical work, Large Eddy Simulations (LES) were used here and the data of Gilchrist and Naughton[1] was used for validation. The focus of this effort was the near field where the largest differences between swirling and non-swirling jets are observed. The validated results are used to assess the changes in the turbulence present when swirl is added. The experiments focused on providing a high quality data set for both near and far field of the jet. A three-component LDA system is used to measure the flow field, and the data obtained is used to evaluate the similarity theory of Ewing[2]. The results indicate that the data behave in a manner consistent with the similarity theory. To date, the computations and experiments have proceeded on parallel paths. However, the computational results have guided the experiments performed, and the current experiment has been consistently modified to ensure a complete validation data set. The use of both experiment and computation for better understanding of turbulent swirling jet flows is just starting.

This report describes the present state of this work. The experimental results to date and comparison with theory are first discussed. The computational approach and important results are then presented. In light of this work, some conclusions and future work are discussed.

# 2 Experimental Work

One of the first goals of the present work was to provide an experimental data set for a range of swirl strengths and distributions that included measurements in both

Table 1: Summary of selected turbulence measurements in swirling jets.

Study	$x/D$	Re	$S$	Type	Diagnostic
Rose[5]	0.2 - 15		0.0, 0.2	Solid Body	HWA
Pratte and Keffler[6]	1.0 - 30	2300	0.0, 0.3	Solid Body	HWA
Morse[7]	0.5 - 20	54-57000	0.25, 0.36	Solid Body	HWA
Elsner and Kurzak[8]	0.0 - 7.5	80000	0.0 - 0.42	q-Type	HWA & 5HP
Mehta et al.[9]	0.19-4.62		0.0 - 0.2	Solid Body	HWA
Panda and McLaughlin[10]	0.12 -2.5	22-57000	0.45, 0.50	q-Type	HWA
Gilchrist and Naughton[1]	1.0 - 19.5	100000	0.0 - 0.23	Solid Body q-Type	HWA & 5HP

the near field and far field that could be used to validate computational simulations and to verify theory. Such a data set was needed since no such data existed at the beginning of this effort. Experiments in swirling jets that included turbulence measurements are listed in table 1. Most of these measurements used hot wires that are no longer the best choice for such measurements in high turbulence intensity flows, and many included a limited domain of measurements as well as limited swirl strengths and distributions. This section first describes the experimental facility and instrumentation used in this study including the three-component Laser Doppler Anemometry system and a traverse built specifically for its use. A brief discussion of the experimental results is then presented and some evidence of the jet behaving like that predicted by similarity theory is presented. A more complete description of the experimental results can be found in the papers by Semaan and Naughton [3] and Semaan et al. [4].

## 2.1 Facility

The swirling jet facility used in this study is capable of producing swirling jet flows with different swirl profiles, swirl strengths, and Reynolds numbers. It was designed specifically for this purpose and produces a swirling jet flow free of artifacts that are found in flows produced by other swirling jet facilities.

The design of the swirling jet facility is described in detail by Gilchrist and Naughton [11], but a general description is provided here. The axial and tangential components are independently injected into the stilling chamber allowing for separate control for each of them. The axial flow is provided by a regenerative blower and passes through baffle plates to ensure that it is evenly distributed across the stilling chamber. To produce the swirling flow, high-pressure air from a compressor is tangentially injected into the stilling chamber through 32 separate injection points that allow for fine control of the tangential velocity profile. The combined flow then passes through four screens to remove any artifacts of the injection and is accelerated through a converging section and a nozzle that provide a 44:1 contraction ratio. A

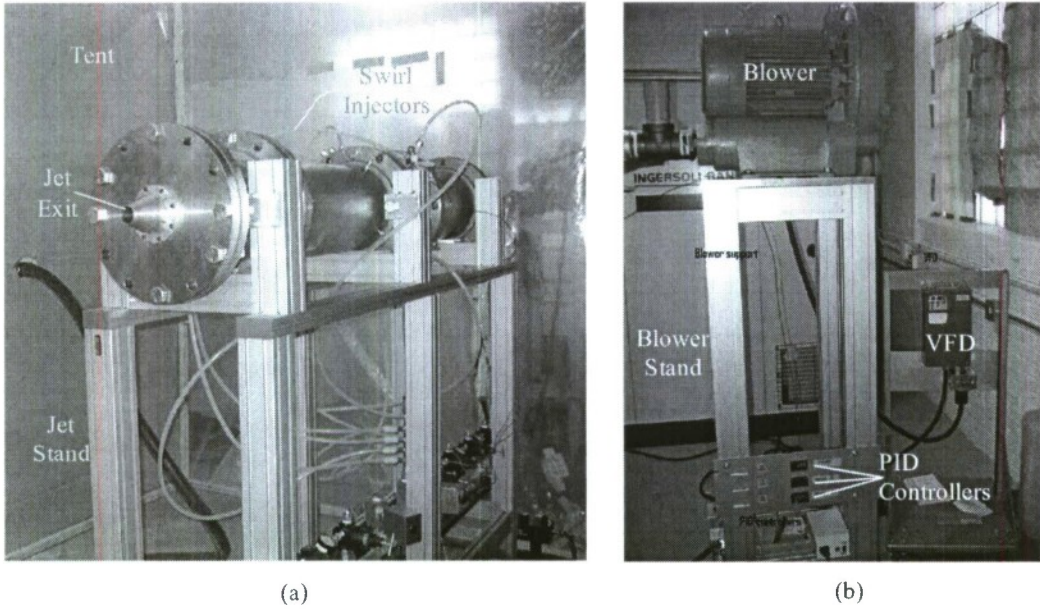


Figure 1: Swirling jet facility with upgrades: (a) jet facility enclosed in tent, and (b) variable frequency drive and PID controllers used to control the jet.

highly conditioned exit flow is produced due to the flow conditioning provided by the screens and large contraction.

The original facility described by Gilchrist and Naughton [11] was significantly upgraded prior to commencing this study to both automate its operation and enable the planned measurements. PID controllers, shown in figure 1(b), regulate the jet temperature and swirl injection pressure through proportional valves. A variable frequency drive was also installed to control the axial mass flow in the jet. In order to minimize flow disturbances, to confine the seeding used for optical diagnostics and to conserve momentum downstream, a tent was erected around the jet. The tent is approximately 14.5 m long, 3.5 m wide, and 3.5 m tall. The dimensions of the tent were selected using a model for the confinement effects, described in Hussein et al.[12], that allowed for the conservation of momentum up to 50 diameters downstream. The jet exit sits approximately 2.6 m from the near end of the tent. Finally, a new stand for the jet was constructed to raise the centerline of the jet to the center of the tent.

Schematics of the swirling jet and its associated coordinate system are shown in Figures 2 and 3, respectively. Note that the velocities shown in the Figure 3 are the axial velocity  $\tilde{u} = U + u$ , the radial velocity  $\tilde{v} = V + v$ , and the tangential velocity  $\tilde{w} = W + w$ , where  $U$ ,  $V$ , and  $W$  are mean velocities, and  $u$ ,  $v$ , and  $w$  are fluctuating velocities.

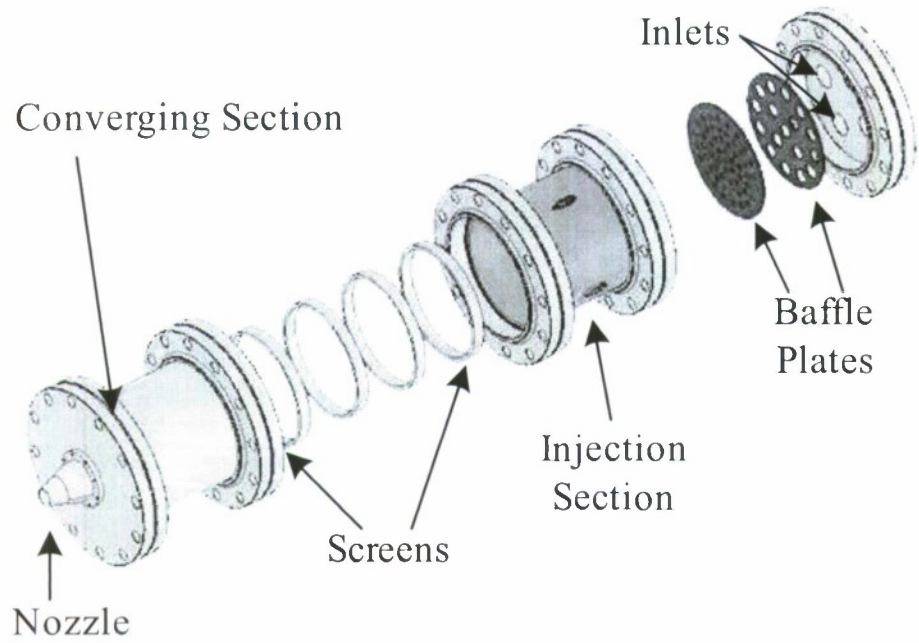


Figure 2: Schematic of the swirling jet facility showing the important components

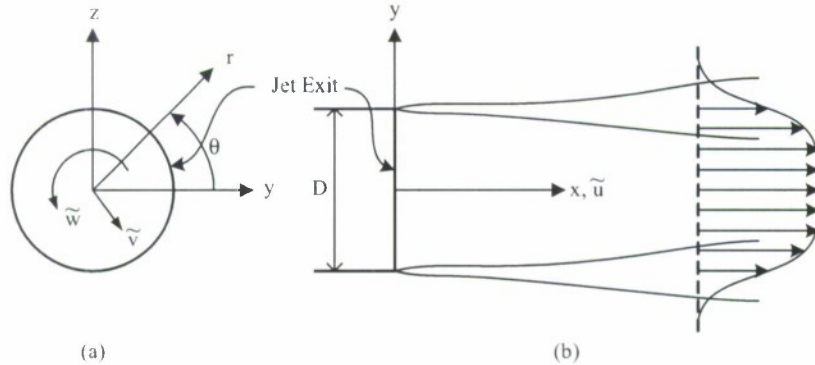


Figure 3: Schematic of swirling jet with coordinate system: (a) looking upstream at the nozzle and (b) looking down on the jet flow from above.

## 2.2 Instrumentation

The system used for the measurements performed here is a TSI three component Laser Doppler Anemometry system. A grant for this system through the National Science Foundation was obtained just as the present study commenced. The system uses a 5W, water-cooled Argon Ion Laser to provide illumination. Light from the laser passes through a color separator that separates the multi-color laser beam into its components (the three components used here were 514.5, 488.0 and 476.5 nm). Each of the colors is further divided in two using a Bragg cell that also shifts one of each beam pair of beams by 40 MHz. The pairs of beams are routed from the

color separator to a transceiver using fiber optic cables where the beams are focused to produce the probe volume. The waist of the measuring volume for each of the beam pairs was 45.64, 43.29 and 42.27  $\mu\text{m}$  for the three channels respectively yielding, after alignment, an effective measuring volume of approximately 40  $\mu\text{m}$  on each side. For the optics used in this study, fringe spacings of 1.917, 1.8183 and 1.7754  $\mu\text{m}$  are produced. Particles passing through the probe volume scatter light that passes back through the transceiver and is focused onto a multi-mode receiving fiber. This scattered light is routed to the amplifier module where the light colors are again separated and focused onto different photo-multiplier tubes (PMTs). Electrical signals from the PMTs are then sent to a burst detector where the signals are processed to determine velocity. As the measurements were done simultaneously in all three components, hardware coincidence was used to guarantee that each data point acquired is real. Hence, a particle crossing the measuring volume needs to produce a signal on all three channels to be accepted. Gate-time time-weighting was enabled throughout the study to reduce the uncertainty caused by the faster particles crossing the measuring volume. When a burst is detected, the pressure and temperature in the stilling chamber are acquired using a 4 channel analog-to-digital converter. Acquisition of the data is controlled by TSI software.

During a survey, the probe volume's location in the flow is determined by positioning the transceivers using an automated three-component traverse. The traverse was designed and built in-house. It is driven by stepper motors connected to independent controllers that are managed by the TSI software, thus allowing for easy control and automation of the surveys. Each stepper motor attaches to a lead screw assembly on its respective axes. The ball-screw assemblies have a 0.2 inch lead on their screws except for the axial-direction screw which have a 0.25 inch lead. This translates to a resolution of 2.54 and 3.175  $\mu\text{m}/\text{step}$  for the respective axes. Two identical linear traverses are used to set the vertical location of the probe volumes ensuring accurate placement.

In three-component LDA measurements, a critical issue is the positioning of the transceivers with respect to each others and to the flow. In the current study, two setups, shown in Figure 4 were used. The first setup was used for near-field measurements since was able to perform measurements at the nozzle exit (and even inside the nozzle) without any obstruction. The disadvantage of this setup is that the calculated velocities are susceptible to uncertainty due to the probes' angular position relative to the jet. The second configuration was used in measurements well downstream of the nozzle exit. The orientation of the probes at 90 degrees relative to the flow axis gave the jet most clearance to grow without any physical interference. One limitation of this configuration is the inability to measure near the exit since the nozzle obstructs two of the six laser beams.

During a typical survey, a relatively sparse survey with limited samples is first taken through the jet to determine the number of samples and sampling duration necessary to obtain a sufficient number of independent samples for a 1% accuracy in the second order quantities. The surveys are then repeated using these settings. Alignment of the two probe volumes was performed before every survey using a pin-hole apparatus. A detailed description of the uncertainty of these measurements can

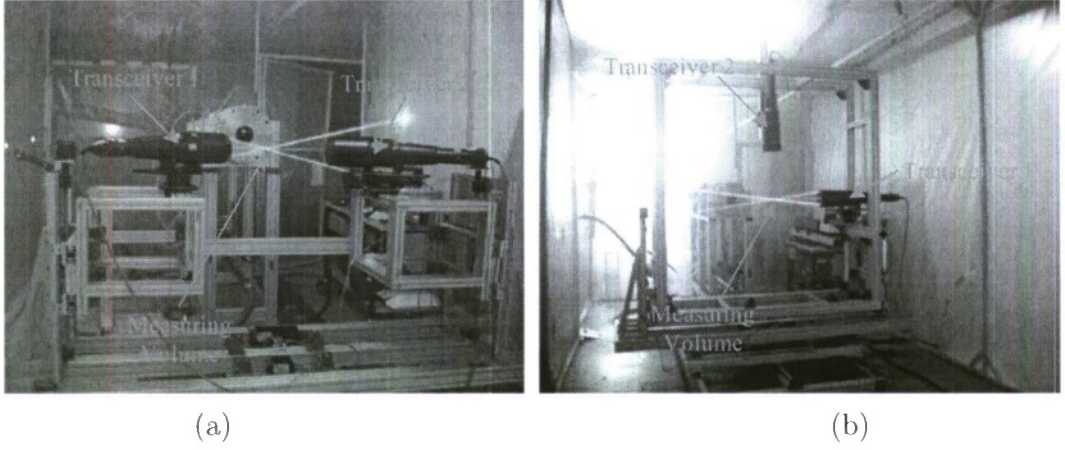


Figure 4: Two different arrangements of the transceivers: (a) both probes approximately 45 degrees to the jet axis, and (b) both probes 90 degrees to the jet axis.

Table 2: Test Cases

Cases	Swirl Number	Re	Tangential Profile	Diameters downstream
(1)	0	114,000	N/A	50
(2)	0.08	109,000	Solid Body	13
(3)	0.21	107,000	Solid Body	50
(4)	0.23	113,000	Q-Vortex	13
(5)	0.39	115,000	Solid Body	11

be found in reference [3].

### 2.3 Test Cases

Three properties best characterize a swirling jet: the swirl number, the swirl distribution and the Reynolds number based on the nozzle diameter. The swirl number is defined as:

$$S = \frac{G_\theta}{M_0 R} , \quad (1)$$

where  $R$  is the nozzle radius,  $G_\theta$  is the angular momentum flux across the nozzle plane:

$$G_\theta = 2\pi \int_0^\infty [UW + \bar{uw}]r^2 dr, \quad (2)$$

and  $M_0$  is the momentum flux across the nozzle exit plane:

$$M_0 = 2\pi \int_0^\infty \rho \left[ U^2 - \frac{W^2}{2} + \bar{u^2} - \frac{(\bar{w^2} + \bar{v^2})}{2} \right] r dr. \quad (3)$$

Two swirl distributions were used in this study: solid-body rotation and the q-vortex. Solid-body rotation is a tangential velocity distribution that grows linearly with radius, whereas the q-vortex has a solid-body core and decays inversely with the radius outside the core. Measurements were made for the two swirl distributions at different swirl numbers, while the Reynolds number was held to  $\sim 100,000$ :

$$Re_D = \frac{UD}{\nu}, \quad (4)$$

with D the nozzle diameter. All the tested cases are listed in Table 2. Measurements were made up to 50 diameters downstream for cases (1) and (3) and to 11 and 13 diameters for the rest of the cases.

## 2.4 Results

Three-component LDA measurements provide the detailed data required for evaluating theory and performing code validation. In this section, a brief example of the data acquired is presented. For a detailed description of the data, see Semaan and Naughton [3].

To demonstrate the effect of swirl on the flow, axial velocity profiles normalized by the exit plane centerline axial velocity for all the cases listed in table 2 are shown in figure 5. As expected, the centerline velocity decays more rapidly in the swirling cases, and the jet widths of those same cases also grow more quickly. Other interesting features to note are the non-top-hat profiles exhibited in the stronger swirl cases.

It is not a surprise that, accompanying the increased momentum diffusion associated with the swirling cases, there are increased turbulence levels near the nozzle exit. Figure 6 shows the axial normal turbulence stresses normalized by the square of the exit plane centerline axial velocity. It can be seen that the higher swirling cases (cases 3-5) exhibit amplified turbulence near the exit plane that decays rapidly with distance downstream. The rapid decay is a result of the weakening in the velocity gradients capable of turbulence production that occurs as both axial linear momentum and angular momentum diffuse.

All six Reynolds stresses are affected by the addition of swirl. As shown in figure 7, the azimuthal normal turbulence stress  $\overline{ww}$  is elevated above the levels observed in non-swirling jets as might be expected from the additional velocity gradient created by the swirl. As with  $\overline{uu}$  and  $\overline{ww}$ , the axial-radial turbulence shear stress  $\overline{uv}$  is also elevated and the other shear stresses become non-zero. To more quantitatively assess these data, a comparison with theory is provided in the next section.

## 2.5 Comparison with Theory

The theory of Ewing [2] demonstrates that the equations governing the incompressible turbulent swirling jet admit a similarity solution. The theory neatly describes how the swirling jet must behave if it is similar. In this general approach, the profiles are described as the product of a normalized profile that is a function of the normalized

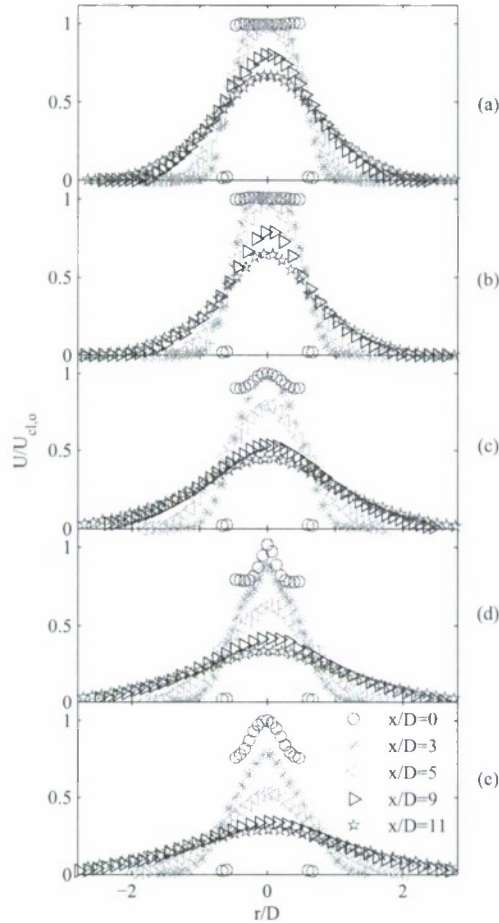


Figure 5: Axial velocity profiles for the different cases: (a) case 1, (b) case 2, (c) case 3, (d) case 4 and (e) case 5.

radial coordinate multiplied by an axially-dependent amplitude. Substituting these profiles into the equations of motion yields a series of constraints that must be met if the jet is to be similar. A summary of the similarity parameters and their constraints is provided in table 3. The results indicate that two items are needed if a profile is to be considered similar: (1) the profiles must collapse when non-dimensionalized appropriately, and (2) the scaling property constraint must be met. Below we consider the swirling jet data in the light of this theory.

Consider whether the axial velocity profile is similar or not. First, the axial velocity profiles must collapse when appropriately scaled. Figure 8 shows the axial velocity profiles for all cases studied, and it is clear that all are collapsing with the swirling cases collapsing more rapidly than the non-swirling cases. To ensure similarity, the constraint on  $U_s$  must also be met. Figure 9 shows the ratio of the spatially depen-

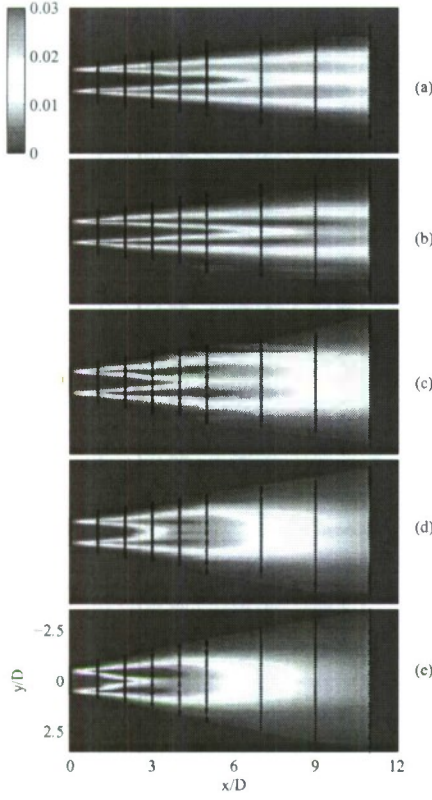


Figure 6: Normalized axial turbulence normal stress  $\bar{u}u/U_{cl,o}^2$  profiles for different cases and different downstream locations: (a) case 1, (b) case 2, (c) case 3, (d) case 4 and (e) case 5.

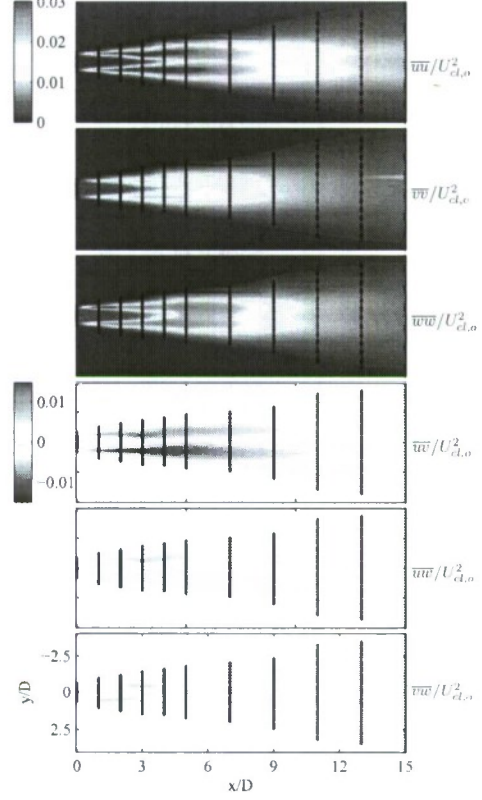


Figure 7: All Reynolds stresses for case 3 normalized by  $U_{cl,o}^2$ .

Table 3: Similarity solutions and constraints for mean velocity and Reynolds stress profiles

Profile	Solution	Constraint
$U(x, r)$	$U_s(x)f(\eta)$	$U_s \propto M_0^{1/2}/b$
$W(x, r)$	$W_s(x)f_\theta(\eta)$	$W_s \propto U_s G_\theta/(bM_0)$
$\bar{u}^2(x, r)$	$K_u(x)k_u(\eta)$	$K_u \propto U_s^2$
$\bar{v}^2(x, r)$	$K_v(x)k_v(\eta)$	$K_v \propto U_s^2$
$\bar{w}^2(x, r)$	$K_w(x)k_w(\eta)$	$K_w \propto U_s^2$
$\bar{u}\bar{v}(x, r)$	$R_s(x)g(\eta)$	$R_s \propto U_s^2(db/dx)$
$\bar{u}\bar{w}(x, r)$	$R_{uw}(x)g_{uw}(\eta)$	$R_{uw} \propto U_s W_S$
$\bar{v}\bar{w}(x, r)$	$R_{vw}(x)g_{vw}(\eta)$	$R_{vw} \propto U_s W_S(db/dx)$

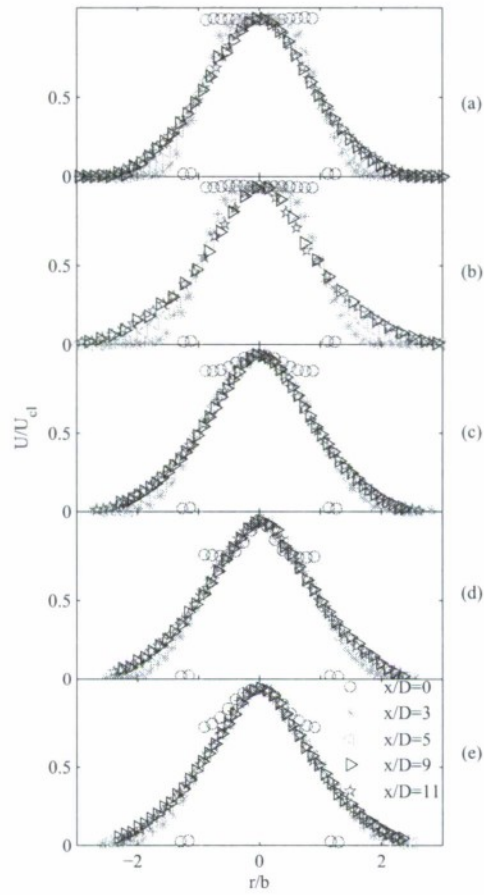


Figure 8: Normalized axial velocity profiles: (a) case 1, (b) case 2, (c) case 3, (d) case 4 and (e) case 5.

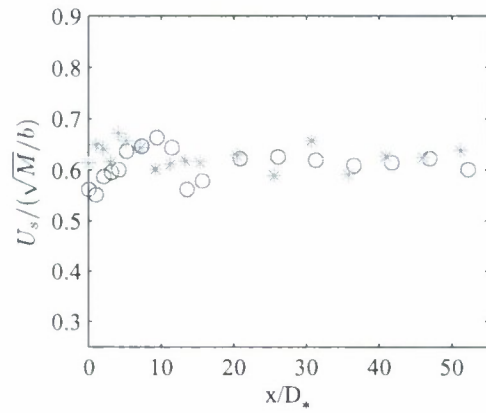


Figure 9: Ratio of  $U_s$  and its scaling vs.  $x/D_*$

dent amplitude of the axial velocity  $U_s$  to the product of the square root of the exit linear momentum and the jet width  $M_0^{1/2}/b$  for cases 1 and 3. As is evident in the figure, this ratio quickly collapses to a constant. The combination of these two results indicates that this jet is acting in a manner consistent with the similarity theory.

A more challenging test of similarity arises with the Reynolds stresses. Figure 10 shows the non-dimensionalized axial normal turbulence stress profiles. In these cases, it is even more evident that the profiles for the swirling jets tend to collapse faster indicating more rapid development and approach to similarity. Although the non-swirling and weak swirling jets do not collapse in the region shown, they do collapse further downstream. Figure 11 shows the ratio of the amplitude for  $\bar{uu}$  divided by the square of the axial velocity scale (here the maximum axial velocity) for cases (1) and (3). Although the data is noisier than desired, it is evident that the swirling jet approaches the asymptotic value more quickly than the non-swirling jet. Nonetheless, they both do approach an asymptotic value thus indicating that the profiles become similar. Analyzing the other turbulent quantities reveals similar results.

Further details of the assessment of the data in light of similarity theory are provided by Semaan et al. [4]. However, the important conclusions are summarized here. First, the swirl-dependent quantities ( $W_s$ ,  $R_{uw}$ ,  $R_{vw}$ ) do decay faster than the other quantities ( $U_s$ ,  $R_{uv}$ ). Taking the ratio of swirl-related quantities to the other quantities (e.g.  $W_s/U_s$ ) shows that the swirl quantities decay by a factor of  $1/x$  faster than the other quantities indicating a de-coupling of the axial momentum and angular momentum as predicted. Further, the experimental data shows that there is a region where the swirl is important and similarity is achieved, which strictly lies outside the region where the similarity theory is valid. The primary effects of swirl are to aid the jet in achieving this similarity faster resulting in a shift of the growth rates and decay rates as indicated by Shiri et al. [13]. Thus, this similarity theory may be used in concert with the experimental data acquired as part of this study to validate computational simulations of this important class of flows.

### 3 Computational Work

The experiments of Gilchrist and Naughton [1] reveal that swirl may have (depending on the swirl number  $S$ ) a significant effect on the growth rate of turbulent jets. Unfortunately, these investigations did not allow for the identification of the mechanisms behind the enhanced growth rates, and thus the means of modifying turbulence structures with swirl is not yet fully understood. Such insight is relevant to the use of swirl for optimizing the enhancement of turbulent mixing in various applications.

Numerical simulations can provide insight into the mechanism of swirling turbulent jets. Reynolds-averaged Navier-Stokes (RANS) methods represent the most efficient methodology for the calculation of turbulent flows, but the use of standard RANS methods for swirling jet flow simulations turned out to be inappropriate [14]. Large eddy simulation (LES) has been proven to be an accurate and computationally feasible approach for turbulent swirling flow simulations [15, 16, 17]. However, there are also questions regarding the realization of such LES. The inflow conditions

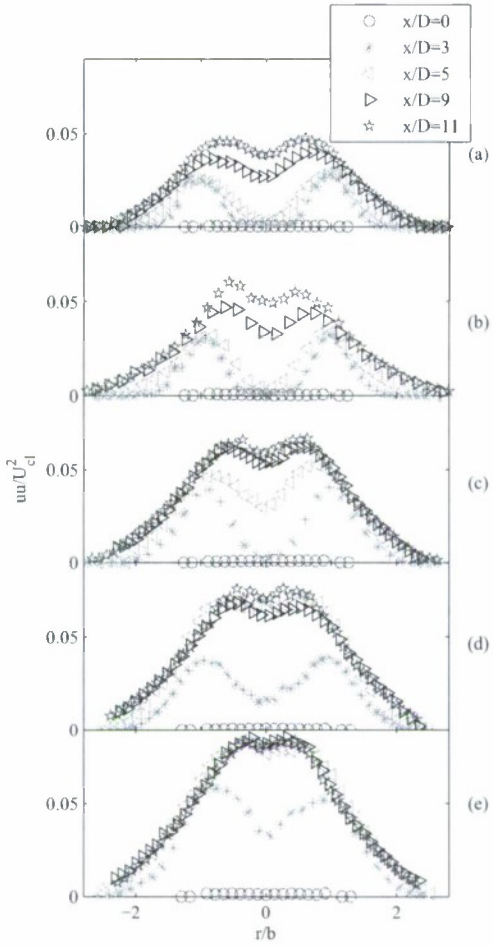


Figure 10: Normalized axial normal turbulent stress profiles: (a) case 1, (b) case 2, (c) case 3, (d) case 4 and (e) case 5.

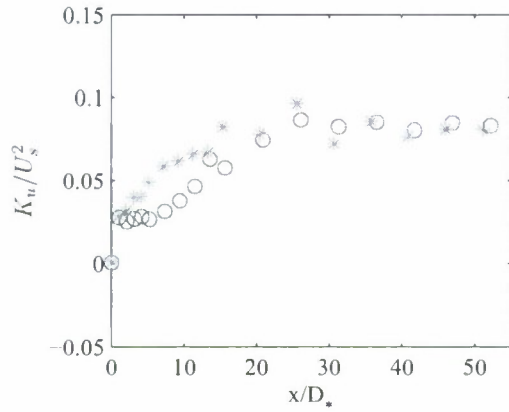


Figure 11: Ratio of  $K_u$  and its scaling vs.  $x/D_*$  for cases (1)  $\circ$ , and (3)  $*$

of jet flows are often determined by a nozzle flow which has a significant influence on the jet flow development. Experimental investigations of flow fields at a nozzle exit often provide incomplete information about inflow data for turbulent swirling flow LES. For example, the dissipation rate of turbulent kinetic energy is difficult to measure, and, as a result, the measurements cannot provide information about the typical length and time scales of inflowing eddies. Unfortunately, LES of the nozzle flow is usually too expensive computationally. Thus, nozzle flow simulations have to be performed on the basis of RANS simulations. The required coupling of RANS simulations and LES involves then the need for a forcing that generates instantaneous inflow data. However, the relevance and optimal generation of such forcing are still unclear [15, 18, 19, 20].

The questions described above were addressed and the data of Gilchrist and Naughton [1] for a non-swirling jet and a jet with a swirl number of  $S = 0.23$  were used to investigate the capability of the LES simulations to capture the important physics present. This evaluation of LES results was performed by using measured data of averaged variables and turbulence statistics. The LES code validated in this way was then used to study the characteristics of a variety of swirling jet flows with swirl numbers ranging from zero to one. The LES data were applied for the analysis of instantaneous velocity and passive scalar fields (the dynamics of coherent structures and the swirl-induced mixing enhancement). The work performed and primary results obtained are summarized here.

### 3.1 Swirling Jet Flow Considered

The effect of different swirl distributions has been investigated experimentally by Gilchrist and Naughton [1]. These investigations revealed significant changes in growth rates, turbulence intensities and the turbulence structures if swirl was added to the flow. These modifications have been attributed to centrifugal instabilities [21]. The geometry of the nozzle and jet flows considered are illustrated in figure 12. Two different swirl profiles have been investigated in the study of Gilchrist and Naughton [22]: one resembling a q-vortex (solid-body core with a free vortex outer region) and the other resembling a solid-body rotation. To generate these different swirl profiles, Gilchrist and Naughton used a unique facility that allows for control of the tangential velocity profile and the creation of a swirling jet that is largely free from artifacts produced by the swirl generation process [1]. For both vortex types measurements of the mean quantities and turbulence statistics are available for swirl numbers  $S = 0.1$  and  $S = 0.23$  at a jet Reynolds number  $Re=1.0 \times 10^5$ . Corresponding data for a non-swirling case are also available. Here, only the non-swirling case and the solid-body swirling case with the swirl number  $S = 0.23$  are considered for comparisons.

### 3.2 LES inflow simulations

To simulate swirling jet flows, one needs inflow data. Unfortunately, experimental data obtained at the nozzle exit do not provide sufficient information to determine the jet inflow conditions. To account correctly for the jet inflow conditions, the best

approach would be to perform LES of both the nozzle and jet flows. However, this approach turns out to be infeasible because of the huge computational cost for LES of the wall-bounded nozzle flow [23]. A way to overcome this problem is to use a combination of RANS and LES methods. RANS simulations are performed to simulate the flow within the nozzle. The profiles of the mean flow variables and turbulence statistics obtained by these RANS simulations are then used as inlet conditions for a LES of the region downstream of the nozzle exit.

Several standard turbulence models were used to perform nozzle flow RANS simulations, but only the shear-stress transport (SST)  $k-\omega$  model [24] provided acceptable results. The RANS simulations were performed on the basis of the FLUENT code [25]. The nozzle flow RANS simulations were shown to be in good agreement with the experimental data at the nozzle exit. It was also shown that the RANS method applied is inappropriate to perform simulations of the region downstream of the jet exit: RANS predictions obtained in this way disagree significantly with the experimental data. The latter observation agrees with the findings of Jakirlic et al. [14].

The results of RANS simulations described in the preceding paragraph were used as inflow data for LES of the jet flows. A significant problem related to LES of swirling turbulent jets is given by the need for fluctuating inflow data [19, 20]. Thus, a forcing mechanism was applied to produce fluctuating velocities at the inlet based on RANS results. In particular, the random flow generation (RFG) technique of Smirnov et al. [18] was used. This method represents a modification of the technique proposed originally by Kraichnan [26]. The advantage of this technique is given by the generation of correlated noise [27, 28] such that the characteristic length and time scales of inflowing instantaneous turbulent eddies are consistent with the corresponding RANS profiles imposed at the inlet. The time dependent fluctuating velocities generated by the RFG method were added to the mean velocity profiles computed by the RANS method. In addition to the forced LES, an unforced LES with non-fluctuating inlet conditions was performed.

### 3.3 Jet flow LES

Several SGS stress models required to close the LES equations were applied: the dynamic Smagorinsky model (DSM) [29], the standard Smagorinsky model (SSM) [30] with a Smagorinsky constant  $C_s = 0.17$ , and the dynamic kinetic energy model (DKEM) [31]. The inflow boundary conditions for velocities are described in section 3. A pressure-inlet boundary condition was used for lateral boundaries, and a pressure-outlet boundary condition was used for the outlet boundary. The transport of a passive scalar was also considered to illustrate the modifications of turbulent mixing due to swirl. An eddy diffusivity model was employed to account for the SGS contribution with a turbulent Schmidt number of 1. The scalar is equal to 1 at the jet inlet and 0 otherwise at the inlet. The scalar value was set to 0 at the lateral boundaries, and zero gradient boundary conditions are applied at the outlet.

The computational domain is conical with a radius of  $1D$  and  $2D$  at the inlet and outlet, respectively. The domain extends up to  $4.1D$  downstream (see figure 12). The domain is discretized into 80 points in azimuthal direction (uniformly distributed),

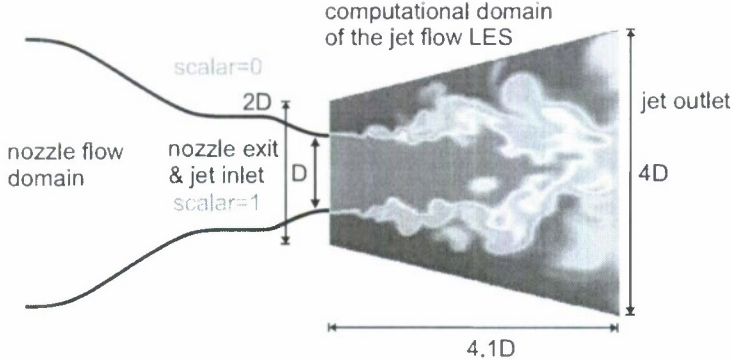


Figure 12: Nozzle design and jet region considered. The solid lines refer to the nozzle body. The nozzle is  $11.65D$  long.  $D = 0.0381\text{m}$  is the nozzle diameter at the exit and  $D_0 = 0.24765\text{m}$  is the nozzle diameter at the inlet. The jet region considered is a conical domain with diameters of  $2D$  and  $4D$ , respectively. The domain length is  $4.1D$ .

Table 4: Numerical setup for the LES jet flows

Simulations	Tools	Settings
Domain		3-dimensional: Conic with length $4.1D$ , radius $1D$ , $2D$ ; divided into 370,000 cells
Solver		Pressure based
SGS models		DSM [29] with $0 \leq C_s \leq 0.23$ ; SSM [30] with $C_s = 0.17$ ; DKEM [31]
Method		Finite volume
Discretization		Bounded central differencing for momentum [25]; SIMPLEC for pressure-velocity coupling

60 points in the radial direction (uniformly distributed) and 80 points in the axial direction with a stretching of 2%. The incompressible LES equations have been solved by a finite volume method based on the CFD code FLUENT [25]. Bounded central differencing is used for the spatial discretization of the momentum equations, a second-order upwind scheme is used for the spatial discretization of the passive scalar equation, and time is advanced via a second-order accurate implicit scheme. The SIMPLEC method is used for the pressure-velocity coupling. Details of the numerical setup are summarized in table 4.

The simulations were run for 15 large eddy turnover times  $t_e = D/U_0$  to eliminate effects of the initial conditions. After this time, the simulations were run for another 920 large eddy turnover times to collect time statistics. Samples are taken every 5<sup>th</sup> time step giving a total of 2,500 samples. Due to the axi-symmetry of the flow an additional averaging of the time statistics over 80 points in the azimuthal direction

has been performed. All averages referred to in this paper have been obtained by this method. All the simulations have been performed on 12 processors of a Beowulf LINUX cluster provided and operated by the Institute of Scientific Computation (ISC) at the University of Wyoming. Obtaining the necessary time statistics required a computational time of about 72 hours.

### 3.4 Forcing and SGS modeling effects

The effects of forcing and SGS modeling were investigated by comparing averaged flows fields with experimental data [1]. The simulation results for the forced LES and unforced LES combined with the DSM for the SGS stress are shown in figures 13, 14, 15, and 16. The non-swirling and swirling solid-body rotation cases are compared in these figures at different downstream positions. In particular, figure 13 shows the radial distribution of the normalized averaged axial velocity  $U/U_0$  and the normalized averaged azimuthal velocity  $W/W_0$ , figure 14 shows the normalized axial velocity fluctuations rms  $u/U_0$ , figure 15 shows the normalized azimuthal velocity fluctuations rms  $w/W_0$ , and figure 16 shows the normalized average static pressure  $P/P_0$ . The mean axial and azimuthal velocities are well represented by the forced LES. There is a minor over-prediction of the intensities of axial and tangential velocity fluctuations. Also, a minor under-prediction of the static pressure is observed. The lack of forcing results in a significant under-prediction of axial velocity fluctuations at  $x/D = 1$ . Hence, the jet growth is under-predicted: see the results for axial velocities. The latter implies steeper mean velocity gradients which produce more turbulence. Therefore, the intensity of axial velocity fluctuations increases strongly which leads to the over-prediction observed at  $x/D = 3$ , and  $x/D = 4$ . Thus, the inclusion of forcing has a positive effect on the resulting predictions.

Results of simulations adopting the DSM, the DKEM, and the SSM for the SGS stress are shown in figures 17 and 18. In particular, these figures show the intensity of axial velocity fluctuations and the static pressure for the non-swirling and swirling cases, respectively. Regarding the non-swirling case, the SSM under-predicts the intensity of axial velocity fluctuations at  $x/D = 1$ . The SSM does not seem to capture the forcing applied at the inlet of the non-swirling jet flow. Overall, the SSM features are similar to the features of the unforced LES. The three SGS models predict almost the same flow fields for the swirling jet. The features of the DSM and the DKEM are the same for both the swirling and non-swirling cases.

Radial distribution of the mean scalar and scalar standard deviation are shown in figure 19. Compared to the swirling case, the mean scalar shows a retarded jet expansion and the scalar standard deviation shows a reduced spreading of the shear layer for the non-swirling case. Hence, the mixing is stronger for the swirling case than for the non-swirling case.

### 3.5 Swirl effects

After comparing averaged velocity and scalar fields with experimental data [1], instantaneous fields will be analyzed now to explain the effects of swirl. An analysis of

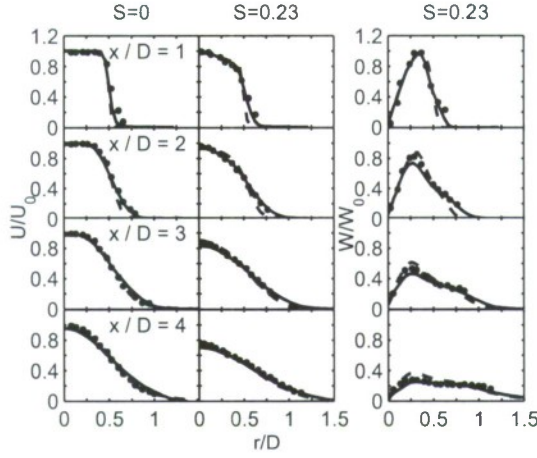


Figure 13: Radial distributions of the normalized averaged axial velocity and tangential velocity for  $S = 0$  and  $S = 0.23$  (solid body) at different axial positions  $x/D$ . Solid lines refer to forced LES results, dashed lines refer to unforced LES results, and symbols denote the experimental data of Gilchrist and Naughton [1]. The normalization data are  $U_0=50.4$  m/s for the non-swirling case,  $U_0=56.3$  m/s and  $W_0=21.7$  m/s for the swirling case.

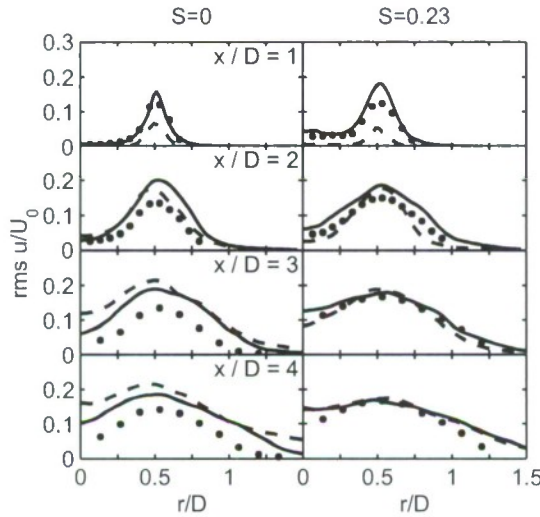


Figure 14: Radial distributions of normalized axial velocity fluctuations for  $S = 0$  and  $S = 0.23$  (solid body) at different axial positions  $x/D$ . Solid lines refer to forced LES results, dashed lines refer to unforced LES results, and symbols denote the experimental data of Gilchrist and Naughton [1]. The normalization data are  $U_0=50.4$  m/s for the non-swirling case and  $U_0=56.3$  m/s for the swirling case.

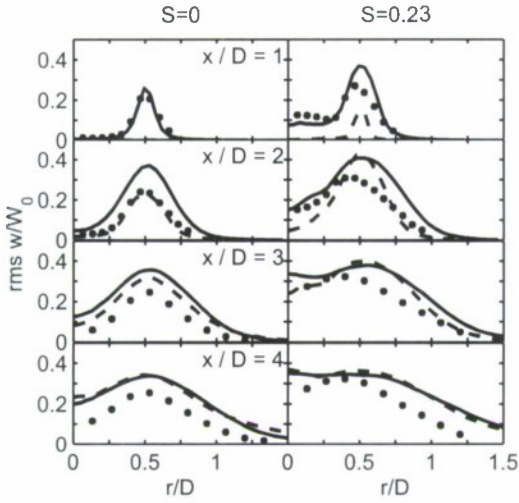


Figure 15: Radial distributions of normalized azimuthal velocity fluctuations for  $S = 0$  and  $S = 0.23$  case at different axial positions  $x/D$ . Solid lines refer to forced LES results, dashed lines refer to unforced LES results, and symbols denote the experimental data of Gilchrist and Naughton [1]. The normalization is given by  $W_0 = 21.7$  m/s.

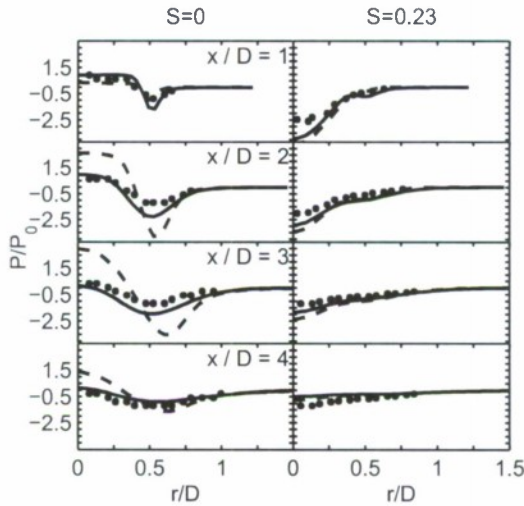


Figure 16: Radial distributions of the normalized averaged static pressure  $P$  for  $S = 0$  and  $S = 0.23$  at different axial positions  $x/D$ . Solid lines refer to forced LES results, dashed lines refer to unforced LES results, and symbols denote the experimental data of Gilchrist and Naughton [1]. The normalization data are  $P_0 = 23$  Pa for the non-swirling case and  $P_0 = 94$  Pa for the swirling case.

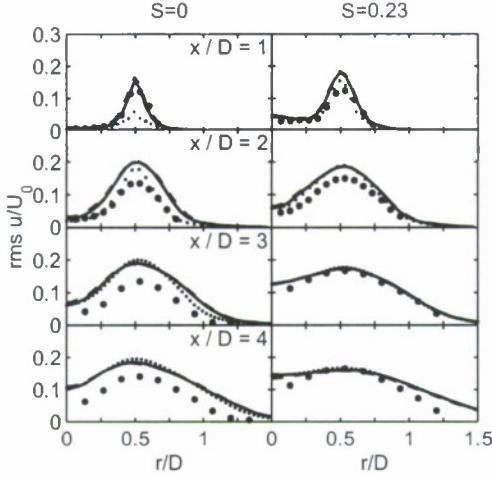


Figure 17: Radial distributions of normalized axial velocity fluctuations for  $S = 0$  and  $S = 0.23$  (solid body) at different axial positions  $x/D$ . Solid lines refer to results of forced LES with the DSM, dashed lines refer to results with the DKEM, dotted lines refer to results with the SSM, and symbols denote the experimental data of Gilchrist and Naughton [1]. Here,  $U_0=50.4\text{m/s}$  for the non-swirling case and  $U_0=56.3\text{m/s}$  for the swirling case.

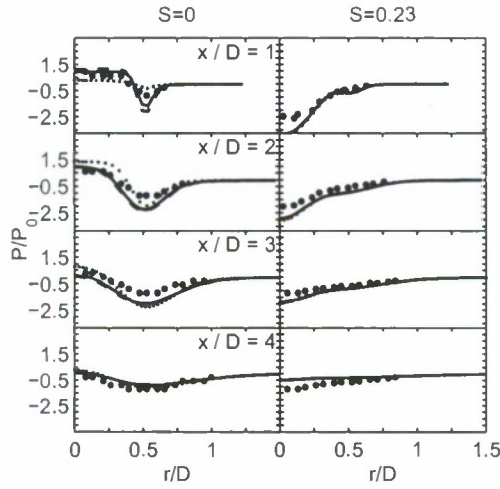


Figure 18: Radial distributions of the normalized averaged static pressure  $P$  for  $S = 0$  and  $S = 0.23$  at different axial positions  $x/D$ . Solid lines refer to results of forced LES with the DSM, dashed lines refer to results with the DKEM, dotted lines refer to results with the SSM, and symbols denote the experimental data of Gilchrist and Naughton [1]. The normalization data are  $P_0 = 23 \text{ Pa}$  for the non-swirling case and  $P_0 = 94 \text{ Pa}$  for the swirling case.

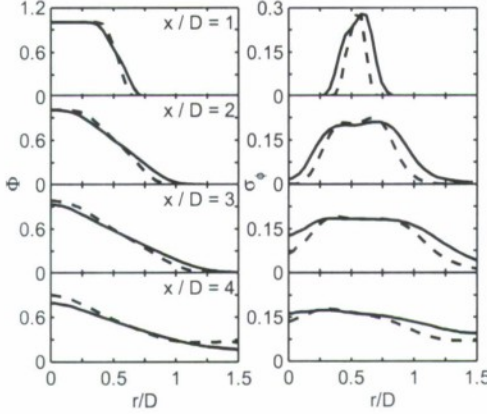


Figure 19: Radial distributions of the averaged scalar  $\Phi$  and the averaged standard deviation  $\sigma_\phi$  of the scalar at different axial positions  $x/D$ . Solid lines refer to the swirling case and dashed lines refer to the non-swirling case.

instantaneous vorticity distributions was used recently by McIlwain and Pollard [15] to support the following idea of swirl effects. Ring structures aligned with the plane normal to the flow form downstream of the jet shear layer due to Kelvin-Helmholtz instabilities. The ring structures collide with stream-wise braid structures. The resulting interaction causes the ring to break apart into smaller, less organized turbulence structures. The addition of swirl increases the number of stream-wise braids, which enhances the breakdown mechanism of the rings. These observations suggest that the increased entrainment observed in swirling flows is due to the action of the braids rather than the rings [15].

Instantaneous vorticity distributions were studied here in accordance to the analysis of McIlwain and Pollard [15]. It was found, however, that these fields do not represent an appropriate means of visualizing coherent structures: the fields obtained did not reveal ring structures. Most likely, the reason for this finding is given by the fact that McIlwain and Pollard's sinusoidal forcing was not applied here but the RFG forcing that generates correlated noise: see section 3.2.

Thus, instantaneous pressure fluctuation fields were considered, which are known to be appropriate for visualizing coherent structures [16, 17]. Figure 20 shows an iso-surface  $\bar{p} - P = -20\text{Pa}$  of instantaneous static pressure fluctuations for the non-swirling and swirling cases. Here,  $\bar{p}$  refers to the filtered pressure and  $P$  is the temporally averaged pressure. The iso-surface is colored according to the filtered scalar  $\bar{\phi} \geq 0.5$  and  $\bar{\phi} < 0.5$ . Figure 20 clearly reveals the existence of ring structures (generated by Kelvin-Helmholtz instabilities) for the non-swirling case. The addition of swirl breaks apart the ring structures into two modes: a helical mode and stream-wise braid structures. The interaction of these two modes generates less organized turbulence structures, which results in enhanced turbulent mixing efficiency. This view of the influence of swirl is similar to that of McIlwain and Pollard. Figure 21 shows a corresponding contour plot of pressure fluctuations along the center-plane

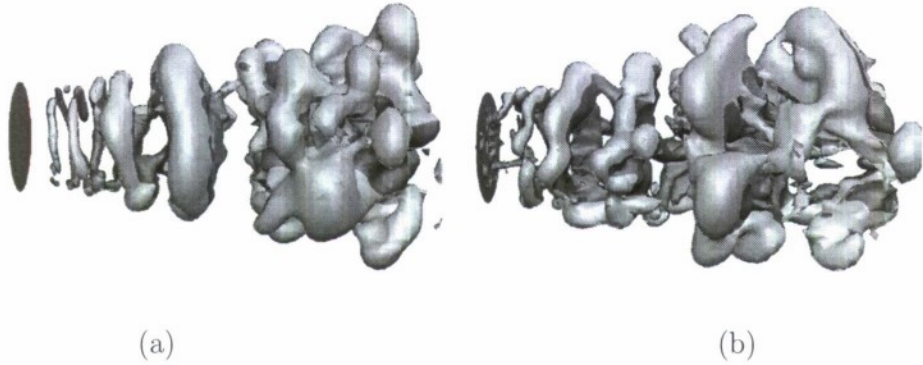


Figure 20: Visualization of coherent vortex structures by means of an iso-surface  $\bar{p} - P = -20\text{Pa}$  of instantaneous static pressure fluctuations: (a) non-swirling case and (b) swirling case. The iso-surface is colored according to the scalar value:  $\bar{\phi} \geq 0.5$  (red) and  $\bar{\phi} < 0.5$  (yellow).

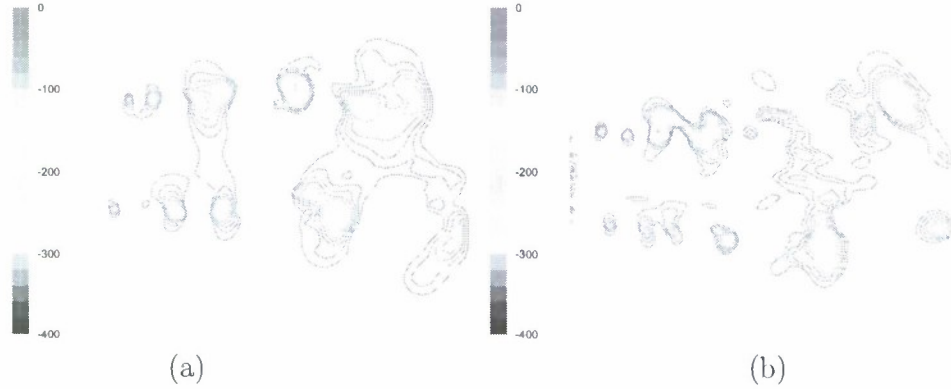


Figure 21: Contour plots of instantaneous static pressure fluctuations  $\bar{p} - P$  in Pa for the non-swirling case (upper picture) and the swirling case (lower picture) along the center-plane  $z = 0$ .

$z = 0$  for the non-swirling and swirling cases. Since the pressure inside a vortex or structure will be low compared to the surroundings, these contour plots can be used to identify the location of the large vortices in the flow. In accordance with figure 20, figure 21 also indicates the breakdown of ring structures. The effect of swirl on the turbulent mixing of passive scalars is illustrated in figure 22 that shows contour plots of instantaneous scalar values in the center-plane  $z = 0$  and in the plane  $x = 1D$ , respectively. This figure clearly shows the increased mixing efficiency due to the enhanced breakdown of ring structures induced by swirl. The addition of swirl increases the number of stream-wise braids, which enhances the breakdown mechanism of ring structures.

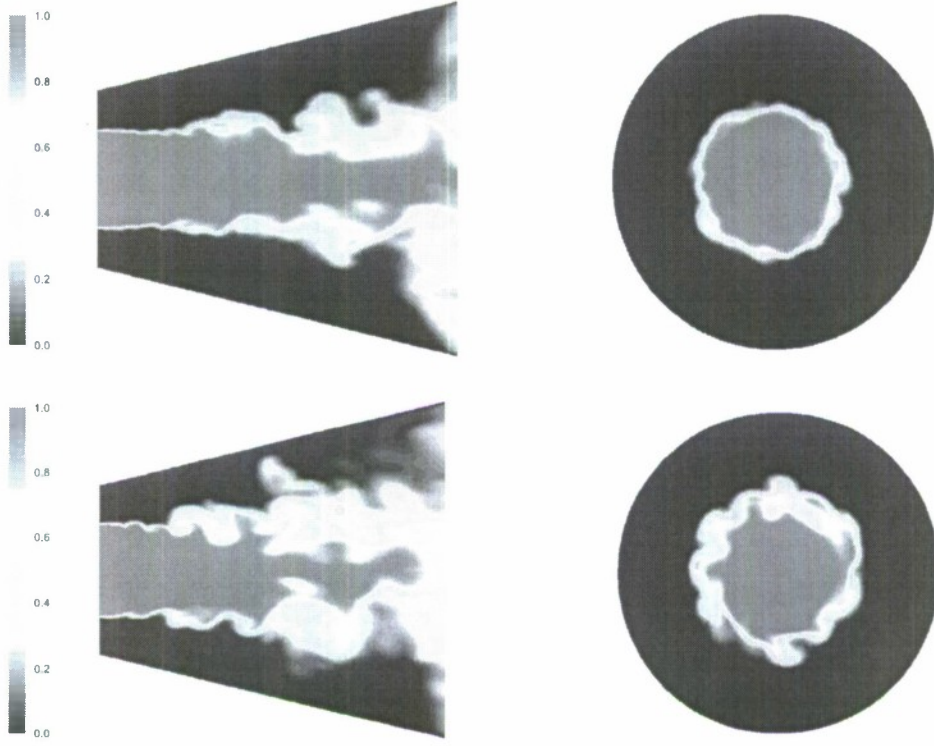


Figure 22: Contour plots of instantaneous scalar values for the non-swirling case (upper pictures) and the swirling case (lower pictures) in the center-plane  $z = 0$  (left) and in the plane  $x = 1D$  (right).

### 3.6 Summary of computational results

The main project objective was to identify the mechanism of swirl effects and to quantify the turbulent mixing enhancement due to swirl. To date, the results have provided essential new insight into these problems.

- First, the analysis of coherent structures reveals that swirl breaks apart the typical coherent ring structures of non-swirling flows into two modes: a helical mode and stream-wise braid structures. The interaction of these two modes generates less organized turbulence structures, which indicates that the efficiency of turbulent mixing is enhanced.
- Second, a detailed analysis [32] of the mixing enhancement caused by swirl shows that the mixing efficiency can be increased by swirl up to a swirl number of about 1. In particular, the global mixing efficiency can be increased by about 20%. This fact is relevant, for example, to the optimization of turbulent combustion systems.
- Third, the realization of the coupling between RANS simulations and LES re-

veals the suitability of the forcing method applied [18]. The advantage of this technique is given by the fact that it generates characteristic length and time scales of inflowing instantaneous turbulent eddies that are consistent with the corresponding RANS profiles imposed at the inlet.

## 4 Conclusions and Future Work

Swirling jet flows of varying strengths and swirl distributions have been considered experimentally and computationally. Laser Doppler Anemometry has been used to provide detailed measurements of the swirling jets. This work provides a data set consistent with earlier results but with a quality and parametric extent suitable for validation of computational models. The data also behaves in a manner consistent with similarity theory of Ewing[2]. Computations using LES have also been performed that agree well with the experimental results of Gilchrist and Naughton[1]. Using the validated approach, several different swirling jet cases have been computed. The results indicate a significant increase in mixing and jet growth that is related to a change in the turbulence structure near the jet exit.

Although integrating computation, experiment and theory has been difficult, the benefits are clear. The computational simulations have been used to guide the experimental campaign, and previous experimental measurements have been used for initial validation of the computations. That computation is now being used to explore the structure of turbulent jet flows for a range of swirl levels. The LDA measurements have been used to demonstrate the applicability of swirling jet similarity theory to at least one swirling flow, and now that theory may also be used to guide experiment and computation for similar swirling flows. However, the real benefits of the experimental and computational results are just being tapped now. The turbulence structure of the jet will be quantified from the computations and used to plan experiments that confirm this structure. The experiments will be used to ensure that the computations are capturing the relevant physics in the jet. With this information, it is hoped that a comprehensive understanding of the effect of swirl on jets will be gained and that this flow and its mechanisms can be exploited for various applications. The integrated approach used here has been the subject of an invited presentation at a conference and has been identified for a special journal issued on integrated approaches to fluid dynamic research.

## 5 Important Collaborations

### 5.1 Chalmers University

In 2005, a collaborative study of the far field of the swirling jet was initiated at Chalmers University while Jonathan Naughton was a visiting faculty member. This work has yielded a better understanding of the far field and resulted in a journal publication with another in development.

## 5.2 Combustion Research and Flow Technology, Inc.

Data from this study and a predecessor are being used by Combustion Research and Flow Technology, Inc. in work related to a SBIR award they have from NASA Marshall. The data are being used to validate swirling flow calculations. The primary contact for this work is Srinivasan Arunajatesan, 6210 Keller's Church Road, Pipersville, PA 18947, (215)766-1520. We hope to continue pursuing this collaboration subject to available funding.

## 6 Personnel

### 6.1 Faculty

The Principal Investigators for this study, **Jonathan Naughton**, **Dan Stanescu**, and **Stefan Heinz**, are members of the faculty at the University of Wyoming. Dr. Naughton has an appointment in the Department of Mechanical Engineering, whereas Drs. Stanescu and Heinz are both members of the Department of Mathematics.

### 6.2 Students

Several students performed work in the support of this study.

- **Celestin Zemtsop** (Dept. of Mathematics, Doctor of Philosophy Candidate) carried out the majority of the simulations reported here. Celestin is expected to receive his Ph.D. in August 2009.
- **Michael Stoellinger** (Dept. of Mathematics, Doctor of Philosophy Candidate) contributed to the simulations reported here through LES code development.
- **Xu Zhang** (Dept. of Mathematics, Post-Doctoral Student) performed code development in support of this project.
- **Richard Semaan** (Dept. of Mechanical Engineering, Doctor of Philosophy Candidate) carried out the Laser Doppler Anemometry measurements reported here. Richard is expected to receive his Ph.D. in August 2009.
- **Bryan Riotto** (Dept. of Mechanical Engineering, Bachelor's of Science) carried out flow visualization measurements of the swirling jet. Bryan graduated in May 2008.

## 7 Publications and Presentations Resulting from this Work

Below are journal articles, conference presentations, conference papers, and theses that are a direct result of the work discussed here. It should be noted that a journal

paper has been requested from one of the talks (Effect of turbulence modification on the near field of swirling jets) for inclusion in a special issue on the fluid information triad. The fluid information triad encourages work that combines computational and experimental tools with the theory to gain the most understanding possible in a particular research effort.

## 7.1 Journal Articles

1. C. P. Zemtsop, M. K. Stoellinger, S. Heinz and D. Stanescu, Large eddy simulation of swirling turbulent jet flows *AIAA Journal*, submitted, 2009.
2. A. F. Shiri, W. K. George, and J. W. Naughton. An experimental study of the far-field of incompressible swirling jets. *AIAA Journal*, 46(8):2002–2009, August 2008.
3. R. T. Gilchrist and J. W. Naughton. An experimental study of incompressible jets with different initial swirl profiles: Mean results. *AIAA Journal*, 43(4):741–751, April 2005.

## 7.2 Conference Papers and Presentations

1. R. Semaan, J. W. Naughton and D. Ewing. Evaluation of turbulent swirling jet similarity theory using LDA measurements. AIAA Paper 2009-1114, January 2009. 47th Aerospace Sciences Meeting, Orlando, FL.
2. C. Zemtsop, M. Stoellinger, S. Heinz and D. Stanescu. Swirl-induced mixing enhancement in turbulent jet flows. AIAA Paper 2009-1510, January 2009. 47th Aerospace Sciences Meeting, Orlando, FL.
3. C. P. Zemtsop, M. K. Stoellinger, S. Heinz and D. Stanescu. Large eddy simulation of swirling turbulent jet flows. In: Proceedings of the 16th Annual Conference of the CFD Society of Canada, edited by D. J. Bergstrom and R. Spiteri, pp. 1-8, Saskatoon, SA, 2008.
4. R. Semaan and J. W. Naughton. Three component LDA measurements in the near and far field of swirling jets. AIAA Paper 2008-761, January 2008. 46th Aerospace Sciences Meeting, Reno, NV.
5. R. Semaan J. W. Naughton and B. A. Riotto. Measurements in the near field of a swirling jet using CTA, LDA, and PLS. AIAA Paper 2007-52, January 2007. 45th Aerospace Sciences Meeting, Reno, NV.
6. C. Zenitsop, M. Stoellinger, S. Heinz, and D. Stanescu. A RANS-LES study of swirling and non-swirling jets. AIAA Paper 2007-925, January 2007. 45th Aerospace Sciences Meeting, Reno, NV.

### 7.3 Conference Presentations (no paper)

1. J. W. Naughton, S. Heinz, and D. Ewing. Effect of turbulence modification on the near field of swirling jets (Invited). AIAA 2008-4388 Oral Presentation in *Further Case Studies in the Fluids Information Triad*, June 2008. 38th Fluid Dynamics Conference and Exhibit, Seattle WA.
2. B. Riotto, R. Semaan, and J. Naughton. Experimental evaluation of swirling jet growth rate enhancement. *Bulletin of the American Physical Society*, 52(17):294, November 2007.
3. R. Semaan and J. Naughton. Three component LDA measurements in swirling jets. *Bulletin of the American Physical Society*, 52(17):294, November 2007.
4. X. Zhang, D. Stanescu, and J. W. Naughton. Application of DNS/LES spectral element methods in turbulent flow simulations. *Bulletin of the American Physical Society*, 52(17):36, November 2007.
5. S. Heinz. Some questions regarding the understanding and prediction of turbulent flow. December 2006. 5th International Conference On Differential Equations and Dynamical Systems, Edinburgh (Texas).

### 7.4 Ph.D. thesis

1. R. Semaan 2009 (expected) LDA measurements in turbulent swirling jets and comparison with similarity theory.
2. C. Zenitsop 2010 (expected) Multiscale modeling and simulation of complex turbulent flows.

## 8 Disclaimer

This work was sponsored by the Air Force Office of Scientific Research, USAF, under grant number FA9550-05-1-0485. The views and conclusions contained herein are those of the authors and should not be interpreted as necessarily representing the official policies or endorsements, either expressed or implied, of the Air Force Office of Scientific Research or the U.S. Government.

## References

- [1] R. T. Gilchrist and J. W. Naughton. An experimental study of incompressible jets with different initial swirl profiles: Mean results. *AIAA Journal*, 43(4):741–751, April 2005.
- [2] D. Ewing. Decay of round turbulence jets with swirl. In W. Rodi and D. Lau-  
rance, editors, *Engineering Turbulence Modeling*, pages 461–470. Elsevier, 1999.

- [3] R. Semaan and J. W. Naughton. Initial assessment of three component LDA measurements for swirling jets. AIAA Paper 2008-761, January 2008. 46th Aerospace Sciences Meeting, Reno, NV.
- [4] R. Semaan and J. W. Naughton. Evaluation of turbulent swirling jet similarity theory using lda measurements. AIAA Paper 2009-1114, January 2009. 47th Aerospace Sciences Meeting, Orlando, FL.
- [5] W. G. Rose. A swirling round turbulent jet. *Journal of Applied Mechanics, ASME Transactions, Series E*, 84:615–625, December 1962.
- [6] B. D. Pratte and J. F. Keffer. The swirling turbulent jet. *Journal of Basic Engineering*, 94:739–748, December 1972.
- [7] A. P. Morse. *Axisymmetric Free Shear Flows with and without Swirl*. PhD thesis, University of London, 1980.
- [8] J. W. Elsner and L. Kurzak. Characteristics of turbulent flow in slightly heated free swirling jets. *J. Fluid Mech.*, 180:147, 1987.
- [9] R. D. Mehta, D. H. Wood, and P. D. Clausen. Some effects of swirl on turbulent mixing layer development. *Physics of Fluids A*, 3(11):2717–2724, November 1991.
- [10] J. Panda and D. K. McLaughlin. Experiments on the instabilities of a swirling jet. *Physics of Fluids*, 6(1):263–276, January 1994.
- [11] R. T. Gilchrist and J. W. Naughton. The design of a swirling jet facility. AIAA Paper 2002-0442, January 2002.
- [12] H. Hussein, S. Capp, and W. George. Velocity measurements in a high-Reynolds-number, momentum-conserving, axisymmetric, turbulent jet. *Journal of Fluid Mechanics*, 258:31–75, 1994.
- [13] A. F. Shiri, W. K. George, and J. W. Naughton. An experimental study of the far-field of incompressible swirling jets. *AIAA Journal*, 46(8):2002–2009, August 2008.
- [14] S. Jakirlic, K. Hanjalic, and C. Tropea. Modeling rotating and swirling turbulent flows: A perpetual challenge (review article). *AIAA Journal*, 40(10):1984–1996, 2002.
- [15] S. McIlwain and A. Pollard. Large eddy simulation of the effects of mild swirl on the near field of a round free jet. *Physics of Fluids*, 14(2):653–661, 2002.
- [16] M. Garcia-Villalba, J. Frohlich, and W. Rodi. Identification and analysis of coherent structures in the near field of a turbulent unconfined annular swirling jet using large eddy simulation. *Physics of Fluids*, 18:1–17, 2006.

- [17] J. Frohlich, M. Garcia-Villalba, and W. Rodi. Scalar mixing and large-scale coherent structures in a turbulent swirling jet. *Flow, Turbulence and Combustion*, 80(1):47–59, 2008.
- [18] A. Smirnov and S. Shi I. Celik. Random flow generation technique for large eddy simulations and particle-dynamics modeling. *Journal of Fluids Engineering*, 123: 359–371, 2001.
- [19] M. Klein, A. Sadiki, and J. Janicka. A digital filter based generation of inflow data for spatially developing direct numerical or large eddy simulations. *Journal of Computational Physics*, 186(2):652–665, 2003.
- [20] C. Bogey and C. Bailly. Effects of inflow conditions and forcing on subsonic jet flows and noise. *AIAA Journal*, 43(5):1000–1007, 2005.
- [21] R. D. Mehta, D. H. Wood, and P. D. Clausen. Some effects of swirl on turbulent mixing layer development. *Physics of Fluids A*, 3(11):2717–2724, 1991.
- [22] R. T. Gilchrist and J. W. Naughton. Experimental study of incompressible jets with different initial swirl distributions: Mean results. *AIAA Journal*, 43(4): 741–741, 2005.
- [23] S. Heinz. Unified turbulence models for les and rans, fdf and pdf simulations. *Theor. Comput. Fluid Dyn*, 21(2):99–118, 2007.
- [24] F. R. Menter. Two-equation eddy-viscosity turbulence models for engineering applications. *AIAA Journal*, 32(8):1598–1605, 1994.
- [25] *FLUENT 6.2 User Guide*. FLUENT INC., Lebanon, NH, 2005.
- [26] R. Kraichnan. Diffusion by a random velocity field. *Physics of Fluids*, 13(1): 245–272, 1970.
- [27] F. Mathey, D. Cokljat, J. P. Bertoglio, and E. Sergent. Assessment of the vortex method for large eddy simulation inlet conditions. *Progress in Computational Fluid Dynamics*, 6:58–67, 2006.
- [28] D. J. Glaze and S. H. Frankel. Stochastic inlet conditions for large-eddy simulation of a fully turbulent jet. *AIAA Journal*, 41(6):1064–1073, 2003.
- [29] M. Germano, U. Piomelli, P. Moin, and W. H. Cabot. A dynamic subgrid-scale eddy viscosity model. *Physics of Fluids*, 3(7):1760–1765, 1991.
- [30] J. Smagorinsky. General circulation experiments with the primitive equations. i. the basic experiment. *Monthly Weather Review*, 91(3):99–164, 1963.
- [31] W.-W. Kim and S. Menon. Application of the localized dynamic subgrid-scale model to turbulent wall-bounded flows. *AIAA-97-0210*, 1997.
- [32] C. P. Zemtsop, M. K. Stoellinger, S. Heinz, and D. Stanescu. Large eddy simulation of swirling turbulent jet flows. *AIAA Journal (submitted)*, 47, 2009.